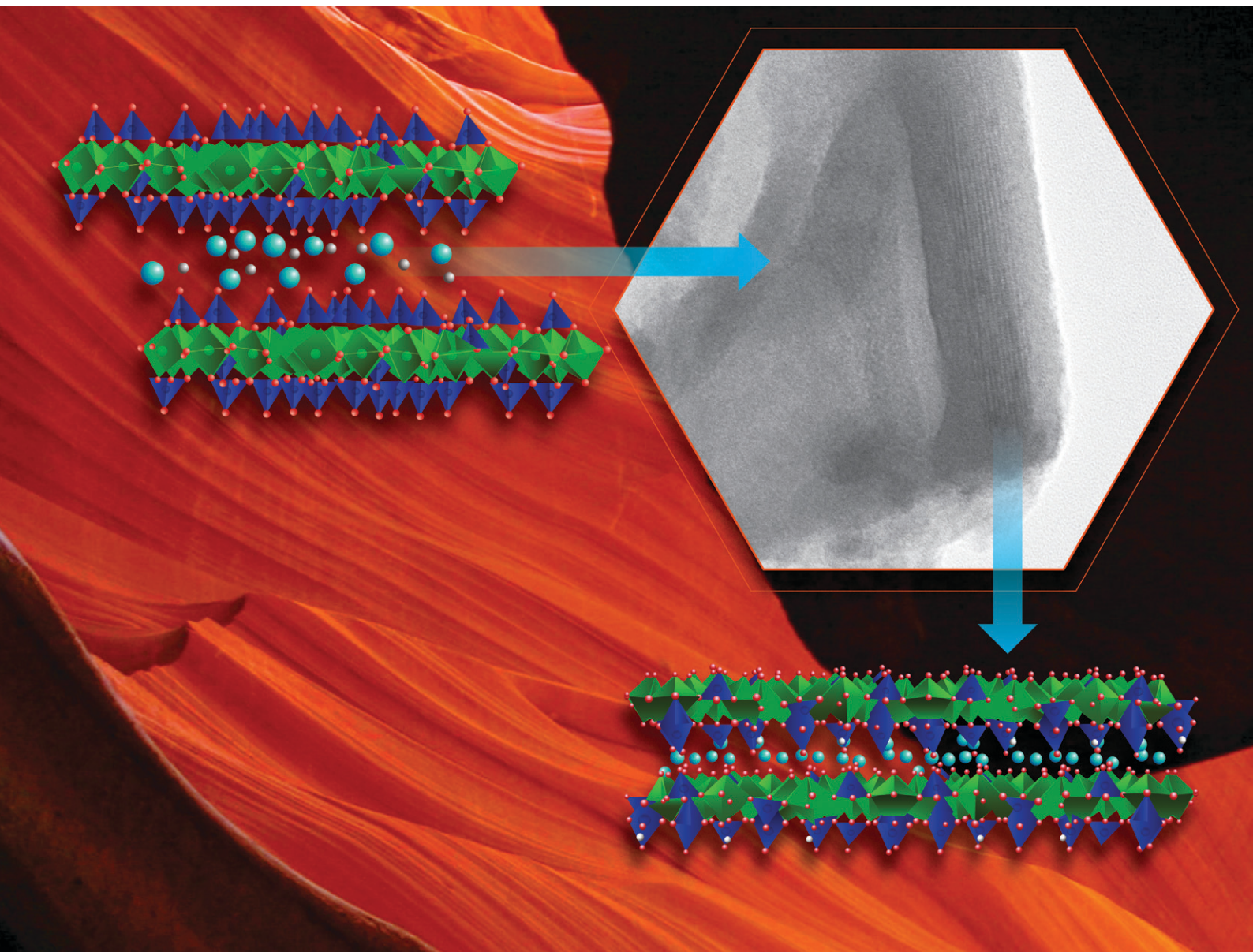


# Environmental Science Nano

Volume 7  
Number 12  
December 2020  
Pages 3631–4034

rsc.li/es-nano



ISSN 2051-8153

## PAPER


Graham King, Mario Alberto Gomez *et al.*  
Revealing the structures and relationships of  
Ca(II)-Fe(III)-AsO<sub>4</sub> minerals: arseniosiderite and yukonite

PAPER



Cite this: *Environ. Sci.: Nano*, 2020, 7, 3735

## Revealing the structures and relationships of Ca(II)–Fe(III)–AsO<sub>4</sub> minerals: arseniosiderite and yukonite†

Graham King, <sup>\*a</sup> Mert Celikin, <sup>b</sup> Mario Alberto Gomez, <sup>\*c</sup> Levente Becze,<sup>d</sup> Valeri Petkov <sup>e</sup> and Giancarlo Della Ventura<sup>f</sup>

The low crystallinity of arsenic (As) containing minerals such as arseniosiderite and yukonite has made a detailed understanding of their atomic structures elusive. X-ray pair distribution function (PDF) and transmission electron microscopy (TEM) were used to gain a detailed understanding of the short and medium-range structural features. High-resolution synchrotron powder diffraction data showed long-range order in arseniosiderite occurs along one direction. PDF data confirmed arseniosiderite has the same general structure as robertsite and mitridatite but with the layers occasionally shifted to disrupt long-range order. Use of small box and reverse Monte Carlo modeling of the PDF data gave the first complete set of atomic coordinates for arseniosiderite. TEM confirmed the degree of interlayer order is generally high. PDF and TEM data show that yukonite is a nano-sized analog of arseniosiderite which lacks any long-range order but is locally similar. The structural evolution of arseniosiderite from yukonite was observed for the first time in a natural specimen *via* TEM. PDF data on several yukonite samples reveal rather sudden drops in the degree of structural correlation as a function of distance. These drops occur from yukonite being composed of small layers made of integer numbers of large nonamers of edge-sharing FeO<sub>6</sub> octahedra, as seen in arseniosiderite. However, these layers are 2 or 3 nonamers in width, with little structural correlation between layers. Thus our work provides a more complete nano/microscopic picture of the key structural features in these minerals found in mining ores and wastes around the world.

Received 13th May 2020,  
Accepted 12th October 2020

DOI: 10.1039/d0en00503g

rsc.li/es-nano

### Environmental significance

The formation and presence of Ca(II)–Fe(III)–AsO<sub>4</sub> minerals in the form of nano-crystalline yukonite and semi-crystalline arseniosiderite has been reported in mining ore deposits and wastes of key resource metals worldwide. Unfortunately, even after 100 years since their discovery, an incomplete understanding of their key structural components remains due to their lower crystallinity. Such an understanding is important to appreciate their formation in natural or anthropogenic settings as well as their observed materials properties (*i.e.* arsenic stability in aqueous systems). Thus our work here *via* high energy diffraction and TEM analysis provides a more complete understanding of their nano and microscopic structural units and how they may relate to their formation as well as observed environmental properties.

## 1. Introduction

Arsenic is a common trace element that is encountered in numerous natural and anthropogenic environments. For example, in gold, uranium, and base metal ore deposits and mine waste around the world [*e.g.* Canada,<sup>1–5</sup> France,<sup>4,6,7</sup> USA,<sup>8–11</sup> Germany,<sup>12</sup> Poland,<sup>13</sup> Portugal,<sup>14</sup> Brazil,<sup>15</sup> Russia,<sup>16</sup> Italy,<sup>5,17</sup> Saudi Arabia,<sup>18</sup> Czech Republic,<sup>19–22</sup> Iran,<sup>23</sup> Uzbekistan,<sup>24</sup> Japan,<sup>25</sup> Australia,<sup>26</sup> and New Zealand<sup>27</sup>], the formation of Ca–Fe(III)–arsenates such as yukonite and arseniosiderite has been reported. The formation of yukonite and arseniosiderite can occur at slightly acidic, and neutral to alkaline<sup>4,28–32</sup> pHs of synthetic or natural solutions that are rich in Ca(II), Fe(III), and As(v) ions. For instance, yukonite

<sup>a</sup> Canadian Light Source, Inc., 44 Innovation Blvd, Saskatoon SK S7N 2V3, Canada. E-mail: graham.king@lightsource.ca; Fax: +1 306 657 3760; Tel: +1 306 657 3535

<sup>b</sup> School of Mechanical and Materials Engineering, University College Dublin, Belfield, Dublin 4, Ireland

<sup>c</sup> Liaoning Engineering Research Center for Treatment and Recycling of Industrially Discharged Heavy Metals, Shenyang University of Chemical Technology, Shenyang LN 110142, China. E-mail: mario.gomez@syuct.edu.cn; Fax: +86 24 83970503; Tel: +86 15140014967

<sup>d</sup> Materials Engineering, McGill University, Montreal, QC H3A 0C5, Canada

<sup>e</sup> Department of Physics, Central Michigan University, Mt. Pleasant, Michigan 48859, USA

<sup>f</sup> Dipartimento di Scienze, Università di Roma Tre, Largo S. Leonardo Murialdo 1, Rome, I-00146, Italy

† Electronic supplementary information (ESI) available. See DOI: 10.1039/d0en00503g

and arseniosiderite may form in natural or anthropogenic environments (e.g. polluted soils and mine wastes) from the oxidation of arsenopyrite,<sup>1,2,6,18,21,25,29</sup> and/or alterations of scorodite,<sup>1,2,28,31</sup> poorly crystalline ferric arsenates,<sup>30,33,34</sup> as well as minerals of the pharmacosiderite group<sup>19,21,29</sup> that exist in gypsum, calcite or Ca-soluble mineral (e.g. anorthite and Ca-montmorillonite) saturated solutions.

All of these reports on the formation of yukonite and arseniosiderite around the world highlight their importance as arsenic-containing and stabilizing mineral phases in natural and anthropogenic environments where abundant CO<sub>2</sub>, highly acidic or basic and strongly reducing conditions are not present that will affect their As and phase stability.<sup>32</sup> In particular, during the hydrometallurgical processing of mineral ores (e.g. gold, uranium and base metals) that contain As poor and Fe rich solutions, As reports to the acidic waste stream effluents whereby it is oxidized first (if not present as As(v)) followed by the addition of Fe(III) (to reach an Fe(III)/As(v) molar ratio  $\geq 3$ ), after which it is neutralized with lime to the desired disposal pH (often pH 7–10) which ultimately leads to the formation of co-precipitate Fe(III)–As(v) phases. Such industrial As-fixation processes lead to the generation of poorly crystalline ferric arsenate, As(v)-ferrihydrite and gypsum waste solids. On the other hand, if acidic waste streams contain As rich and poor Fe deficient solutions then the formation of scorodite under autoclave or atmospheric conditions is preferred which generates solid wastes in the form of scorodite and gypsum.<sup>33</sup> Disposal of such co-precipitate Fe(III)–As(v) and scorodite phases in tailings ponds from hydrometallurgical industries saturated in gypsum or Ca-containing soluble phases (e.g. calcite, lime, anorthite, Ca-clays) in turn may cause the formation of yukonite and arseniosiderite. These Ca(II)–Fe(III)–AsO<sub>4</sub> mineral phases may then serve as secondary alteration As control phases (dependent upon environmental conditions) upon the transformation of these Fe(III)–As(v) waste solids formed with time.<sup>1–3,6,11,24,33</sup> Under natural geological settings, yukonite and arseniosiderite may also serve as secondary As immobilization control phases from the oxidation or alteration of Fe–S–As and Fe(III)–As(v) phases that may dissolve or change over time from perturbations (e.g. pH, E<sub>h</sub>, temperature, PCO<sub>2</sub>, plumes of Fe(III)<sub>(aq)</sub>–Ca(II)<sub>(aq)</sub>–As(v)<sub>(aq)</sub>) caused in their environment.<sup>5,15,17–19,22,23</sup>

To date, a full structural picture of yukonite, a nano-crystalline mineral, and its semi-crystalline analog, arseniosiderite, remains unknown even 100 years after their discovery. Some reports in the literature from various research groups have explored their structures from a chemical (inductively coupled plasma optical emission spectrometry-ICP-OES, electron microprobe analysis-EMPA), molecular (*via* infrared-IR and Raman), structural (*via* lab-based X-ray diffraction-XRD and transmission electron microscopy selected area electron diffraction-TEM-SAED) and short-range order (*via* the use of X-ray absorption near edge spectroscopy-XANES, and extended X-ray absorption fine structure spectroscopy-EXAFS) perspective.

The chemical composition, stoichiometry, and corresponding formulae reported in the literature<sup>1–5,12,13,16,28,32,34</sup> for both arseniosiderite and yukonite has a large range of variation in terms of Ca, Fe, AsO<sub>4</sub>, and H<sub>2</sub>O content (Tables S1 and S2†). The exact reasons for this large variation are still unknown but likely arise from the fact that a lack of a definitive crystal structure which would then confine a unique crystallochemical formulae remains elusive<sup>32</sup> due to their nano to micro-crystalline nature. The molecular structure of arseniosiderite<sup>4</sup> was shown to have two distinct H-bonding networks and was proposed to be one of the key features allowing it to possess a long-range structure similar to mitridatite (Ca<sub>6</sub>(H<sub>2</sub>O)<sub>6</sub>[Fe<sub>5</sub>O<sub>6</sub>(PO<sub>4</sub>)<sub>9</sub>].3H<sub>2</sub>O).<sup>35</sup> Furthermore, the presence of well-ordered AsO<sub>4</sub>, OH, and H<sub>2</sub>O molecular units in comparison to yukonite were also observed in addition to the protonated HAsO<sub>4</sub> group.<sup>4,21</sup> In contrast, yukonite exhibited only one distinct diffuse disordered type of H-bonding network which authors have proposed to be one of the leading causes of its short-range order and are in agreement with the fact it is also a Ca-deficient analog of arseniosiderite.<sup>4,28</sup> It is worth noting that Ca-dimers [Ca<sub>2</sub>O<sub>10</sub>(H<sub>2</sub>O)<sub>2</sub>] parallel to the *a*-axis form intermolecular H-bonding networks that connect P–Fe/Mn tetrahedral–octahedral sheet layers in mitridatite and robertsite(Ca<sub>3</sub>Mn<sub>4</sub>[(OH)<sub>3</sub>|(PO<sub>4</sub>)<sub>2</sub>].3H<sub>2</sub>O)<sup>35,36</sup> to give its repeating long-range structure. Local short-range atomic molecular structure observed *via* XANES (tens of Å) and EXAFS ( $\leq 5$  Å) was found to be nearly identical in both yukonite and arseniosiderite in terms of bond lengths and coordination numbers.<sup>4,28</sup> Furthermore, As and Fe K-edge EXAFS<sup>28</sup> has indicated that yukonite and arseniosiderite precursor particles formed were composed of undistorted oligomeric units of edge-sharing FeO<sub>6</sub> octahedra and bridging AsO<sub>4</sub> molecules. Meanwhile, the local As and Fe structures of intermediate and final precipitates determined by EXAFS<sup>28</sup> were postulate to be compatible with that of mitridatite.<sup>35</sup>

TEM imaging has shown arseniosiderite to consist of thin flat plate micron-sized crystal particles growing with preferential elongation to the (002) plane with corresponding lattice fringes of 5.4 Å. Meanwhile, SAED has shown single-crystal hexagonal diffraction lattice domains.<sup>4</sup> In distinction, yukonite is a nano-domain ordered material whose nano-crystallites have reported sizes of 5, 15, 50, and  $\geq 100$  nm showing internal lattice order over 1–15 nm.<sup>4,5,16,28</sup> Interestingly, high magnification images have shown yukonite to be also composed of lamellar thin flakes/sheets with lath-shaped nano-crystals having irregular lattice fringes corresponding to the (100) plane of arseniosiderite that is bent, curved, and polygonized.<sup>5,16,28</sup> The majority of yukonite SAED<sup>4,5</sup> has shown only weak to strong diffractions rings typical of polycrystalline materials. However, one study<sup>16</sup> of a hydrothermally formed yukonite has reported single-crystal diffraction images and suggested that the plate crystals have mainly an orthorhombic C-centered symmetry but some were also hexagonal. Because this is the only study to ever report

such single-crystal ED patterns, other authors have questioned whether impurities from arseniosiderite may have been present in this study.<sup>4,32</sup>

Crystallographic reports of phosphate analogs to arseniosiderite such as robertsite (RB) and mitridatite (MT) based on single crystals exist in the literature.<sup>35,36</sup> Reports of these structures have indicated them to consist of  $[(M_9O_6(XO_4)_9)^{-12}]$  where  $M = Mn(III)$  or  $Fe(III)$  and  $X = As(V)$  or  $P(V)$  compact sheets that are oriented along the  $a$ -axis. The sheets are composed of  $[MO_6]$  octahedral units that share edges to form 9-member pseudo-trigonal rings that pack in mono-layers. At the center of the nonamers, their corners, and above/below its plane there exist nine distinct crystallographic  $XO_4$  molecules that hold together the sheets of 9 member  $[MO_6]$  octahedral rings. These  $[M_9O_6(XO_4)_9]^{-12}$  sheets are stacked along the  $a$ -axis by water molecules and layers of  $[Ca_2O_{10}(H_2O)_2]$  dimers that destroy the trigonal symmetry and lead to the monoclinic cell reported for RB and MT. Along these layers parallel to the  $a$ -axis,  $CaO_5(H_2O)_2$  polyhedra in the dimers contribute two strong and one weak H-bonding network to the  $XO_4$  molecules of the sheets that result in a perfect basal cleavage parallel ( $\parallel$ ) to the  $a$ -axis. Nevertheless, no specific information exists for arseniosiderite whose crystal structure has largely been assumed to be analogous to MT and RB. Furthermore, even simple space group assignments of the arseniosiderite mineral are unclear to date as can be seen from the CIF files reported in the American Crystallographic Database and the existing literature reports that list them belonging to the  $Aa^{35,36}$  and/or  $A2/a^{37,38}$  space groups.

Therefore, because of the importance of yukonite and arseniosiderite in natural and anthropogenic environments and the lack of complete nano and full crystallographic information for these minerals, we undertook a detailed structural investigation of synthetic and natural samples. The aim of this study is at addressing in detail the degree of structural (but not the elemental/compositional) variation that may occur in these compounds. This task was accomplished *via* the combination of advanced synchrotron X-ray diffraction through the standard Bragg diffraction, pair distribution function (PDF) analysis coupled with reverse Monte-Carlo modeling, and TEM-SAED. Our work presented here is meant to give a more complete picture of yukonite and arseniosiderite at the nano and micro-scale for the user community to be able to employ in their respective work where such Ca-Fe(III)-arsenates are often encountered.

## 2. Experimental

### 2.1 Synthesis and origins of natural yukonite and arseniosiderite samples

Six yukonite samples were studied, 1 synthetic ( $Ca_2Fe_3(AsO_4)_3(OH)_{10} \cdot 5H_2O$ ) and 5 natural mineral samples. The synthetic yukonite (Syn yukonite) was made based on previous work.<sup>4,39</sup> Briefly,  $1.4 \text{ g L}^{-1}$  of As(V) in the form of  $Na_2HASO_4 \cdot 7H_2O$  was dissolved in deionized (DI) water

followed by pH adjustment to approximately 0.5 with  $HNO_3$ . After which the appropriate amount of  $Fe_2(SO_4)_3 \cdot 5H_2O$  and  $CaSO_4 \cdot 2H_2O$  were added to the arsenic-containing solution to give a Ca/Fe/As molar ratio of 0.5/0.75/1. This solution was then agitated for 24 h at room temperature. Subsequently, the solution was heated to 95 °C under agitation (300 rpm) and its pH value was brought to 8 in about 15 minutes using sodium hydroxide (NaOH). During aging, the pH was kept constant at 8 by the addition of NaOH or  $HNO_3$  as needed. At the end of the synthesis, the precipitate was filtered with 0.1  $\mu\text{m}$  pore size membranes in a pressure filter at 50 psi and washed with DI water before drying ( $T = 50 \text{ }^\circ\text{C}$ ) and subsequent characterization. Four of the natural samples were from Tagish Lake in Canada. The first yukonite mineral sample (NMCC yukonite) was in a single solid piece form (National Mineral Collection of Canada, Ref. # 064815) and was collected in 1984 from Venus mine, Windy Arm, Tagish Lake, Yukon Territory. Two other Tagish lake samples were provided by the London Natural History Museum (Ref. BM.1924,972), one of which was a lighter color (LNH light yukonite) and the other one was a darker color (LNH dark yukonite). The third yukonite sample (GdM yukonite) was obtained from the prehistorically exploited copper-iron mine at Grotta della Monaca cave, Sant'Agata di Esaro, Cosenza, Italy.<sup>5</sup> The fourth yukonite sample (ROM yukonite) was obtained from the Venus mine in the Yukon Territory and was donated by the Royal Ontario Museum in Toronto (Ref. # M37256). Two arseniosiderite samples were studied. One is a naturally occurring mineral sample (Ref. # BM 68062) from the Romaneche-Thorins region of France donated by the Natural History Museum in London (LNH arseniosiderite), while the other was synthetically produced (Syn-arseniosiderite). The synthetic arseniosiderite was produced similarly with the same Ca/Fe/As molar ratio as the synthetic yukonite noted above. The only exception being that the heating period was done in a 2 L-Parr autoclave equipped with a glass liner. The solution was heated to 160 °C and held there for 24 h while continuously stirred at 300 rpm. At the end of the synthesis period, the solids were treated similarly as the yukonite noted above.

### 2.2 Synchrotron powder diffraction

High-resolution powder diffraction data were collected on the LNH arseniosiderite sample on beamline 11-BM of the Advanced Photon Source using  $\lambda = 0.420234 \text{ \AA}$  radiation. The total scattering data that was primarily analyzed was collected on the Brockhouse high energy wiggler beamline at the Canadian Light Source using a wavelength of  $\lambda = 0.210515 \text{ \AA}$  (nominally 60 keV). Data was collected on the naturally occurring LNH arseniosiderite sample (Ref. # BM 68062), the light and dark LNH yukonite samples (Ref. # BM 1924,972), the Grotta della Monaca cave, and ROM yukonite samples. The data was processed using GSAS-II.<sup>40</sup> The  $Q_{\text{max}}$  used to produce the PDF of the arseniosiderite sample was  $22.9 \text{ \AA}^{-1}$

while a  $Q_{\max}$  of  $21.7 \text{ \AA}^{-1}$  was used to produce the PDFs of the four yukonite samples. The instrumental dampening function  $Q_{\text{damp}}$ , as defined in the PDFgui software, was determined by fitting the PDF of a Ni sample collected under the same experimental conditions. The fairly small value of 0.0281 for  $Q_{\text{damp}}$ , allows the structures to be probed out to  $\sim 100 \text{ \AA}$ . Supplemental total scattering data was also collected on beamline 11-ID-C of the Advanced Photon Source using  $\lambda = 0.1076 \text{ \AA}$  radiation (nominally 115 keV) on the Synarseniosiderite sample, Syn-yukonite, and the NMCC yukonite (Ref. # 064815). Modeling of the PDF data was done with PDFgui and RMCProfile.<sup>41,42</sup>

### 2.3 Transmission electron microscopy (TEM)

Selected area electron diffraction (SAED) analysis was conducted on both LNH yukonite and LNH arseniosiderite samples with a FEI Tecnai G2 20 Twin TEM using 200 kV. Samples were broken into small pieces and the particles deposited onto carbon (C)-film coated TEM Cu-grids. Upon conducting morphological analysis, Kikuchi maps are used to tilt the specimen to obtain electron diffraction patterns (DPs). High-resolution imaging was also conducted to determine lattice spacings.

## 3. Results and discussion

### 3.1 Powder diffraction analysis

As a first step, high-resolution synchrotron powder diffraction data were collected on the LNH arseniosiderite sample to see if it would be possible to solve the crystal structure. The diffraction pattern is shown in Fig. 1. Most of the observed peaks can be indexed using the same  $Cc$  monoclinic unit cell reported for robertsite and mitridatite.<sup>35,36</sup> A few very sharp peaks can be attributed to a small amount of  $\text{SiO}_2/\text{quartz}$ . While some of the arseniosiderite peaks are fairly sharp, some are very broad

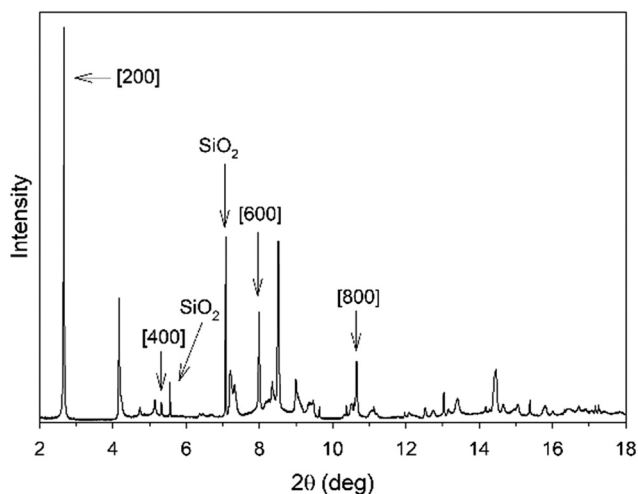


Fig. 1 High-resolution synchrotron powder diffraction pattern of the natural LNH arseniosiderite sample.

and other peaks that would be expected from such a unit cell are completely absent. In general, the  $h00$  peaks were quite sharp, being only slightly broader than the  $\text{SiO}_2/\text{quartz}$  peaks. Many other peaks are present but are difficult to resolve as they are very broad and heavily overlap. A few expected peaks were completely absent, particularly all those with  $h31$  or  $h33$  indices. These absences could indicate higher symmetry or a smaller unit cell. However, no satisfactory new cell could be found and a new unit cell would also not explain the broadness of many of the peaks. These observations can be interpreted as arseniosiderite having the mitridatite structure type but lacking long-range correlation in some directions. As the  $a$ -lattice parameter is the one perpendicular to the layers, the sharpness of the  $h00$  peaks indicates a regular inter-layer spacing. The broadness or absence of the other peaks indicates an absence of long-range correlations among atoms in different layers, suggestive of the layers being randomly shifted within the  $bc$ -plane relative to each other. This disorder makes it impossible to perform a conventional structure determination from powder diffraction data.

### 3.2 PDF analysis of arseniosiderite

To circumvent the problem of low crystallinity and gain more details on the short and medium-range order, the PDF method was used. As can be seen in Fig. 2a, the PDF of the naturally occurring arseniosiderite sample extends beyond  $100 \text{ \AA}$ . The PDF of the synthetic sample looks quite similar but falls off more quickly due to greater instrumental dampening (Fig. S1†). The low- $r$  features, seen in Fig. 2b, can be assigned to specific inter-atomic distances.<sup>43</sup> The peak at  $1.69 \text{ \AA}$  can be assigned to tetrahedral As–O bond distances, while the peak at  $2.05 \text{ \AA}$  is from octahedral Fe–O bond distances. The broad peak around  $2.42 \text{ \AA}$  is from Ca–O bond distances while the weak, broad feature around  $\sim 2.7 \text{ \AA}$  is due to O–O distances. The next strong peak contains contributions from several types of cation–cation distances. The low- $r$  shoulder around  $3.2 \text{ \AA}$  occurs due to Fe–Fe distances between edge-sharing  $\text{FeO}_6$  octahedra, while the Fe–Fe distances due to corner shared  $\text{FeO}_6$  occur around  $3.5 \text{ \AA}$ . Fe–As distances occur around  $3.4 \text{ \AA}$  while Ca–Fe is around  $3.5 \text{ \AA}$ , and Ca–As is around  $3.8 \text{ \AA}$ .

The initial fitting of the data was done using a unit-cell like description with the program PDFgui. The mitridatite structure was used as a model by replacing P with As. The unit cell is expected to expand significantly when the larger As ( ${}^4\text{P}^{5+} = 0.17 \text{ \AA}$  vs.  ${}^4\text{As}^{5+} = 0.335 \text{ \AA}$ )<sup>44</sup> is present. A unit-cell with a composition of  $\text{Ca}_2\text{Fe}_3(\text{AsO}_4)_3 \cdot 3\text{H}_2\text{O}$  was used in the fitting. To refine the unit cell, the data was fit over an  $r$ -range of  $2.8\text{--}40 \text{ \AA}$ . From this fitting lattice parameters of  $a = 18.128 \text{ \AA}$ ,  $b = 19.925 \text{ \AA}$ ,  $c = 11.542 \text{ \AA}$ ,  $\beta = 95.92^\circ$  were obtained. The  $a$ -parameters showed the largest increase relative to the mitridatite unit cell, followed by the  $b$ -parameter, and the  $c$ -parameter. The fit is fairly good and confirms that arseniosiderite does belong to this structure type (Fig. S2†). However, there are some minor issues with the peak

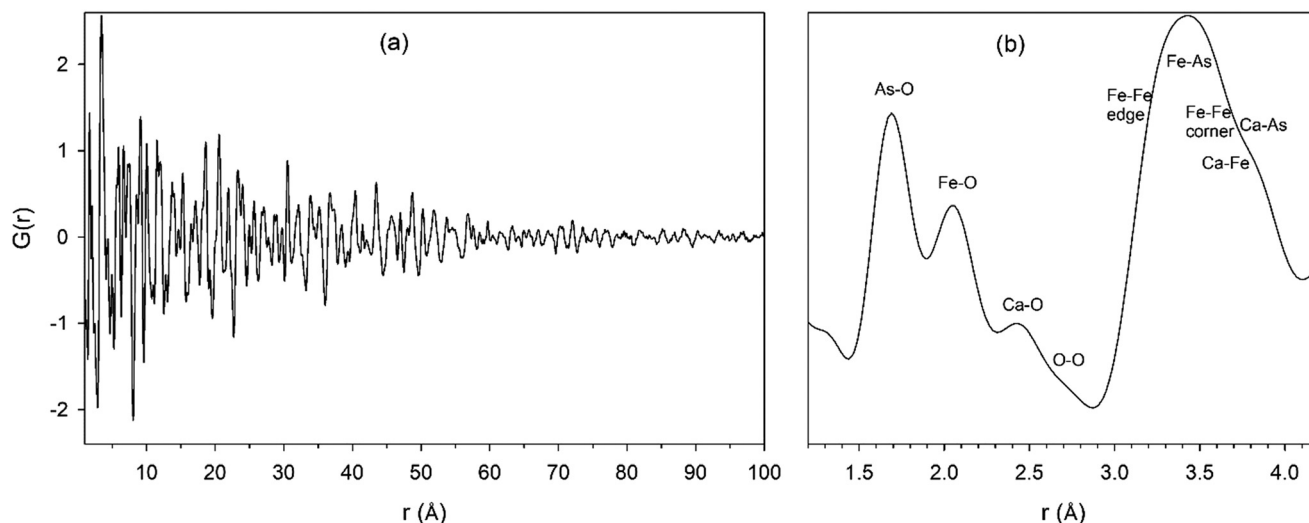


Fig. 2 The PDF of the LNH arseniosiderite sample out to 100 Å (a) and over nearest neighbor distances (b).

positions and intensities, since the bond distances change some when As, replaces P.

The very large number of degrees of freedom for this structure type (225 for atomic positions alone) precludes a full structural refinement using PDFgui. However, the reverse Monte Carlo (RMC) approach can be used to fit the experimental PDF. To generate a starting model, the unit cell of mitridatite was used but P was replaced with As, and the unit cell parameters were set to those obtained from the PDFgui fitting. This unit cell was expanded into a  $5 \times 5 \times 8$  supercell containing 60 000 atoms. To enable fitting out to an  $r$ -value of 42 Å, the experimental  $G(r)$  was multiplied by the inverse of the instrumental dampening function. The RMC simulation was run for several days against the  $G(r)$  until convergence was reached. As the peaks from As–O, Fe–O, and Ca–O bonds significantly overlap, bond valence constraints were used for As, Fe, and Ca atoms to ensure the resulting configuration both fit the experimental data and had realistic distributions of bond lengths.

The fit using the RMC method is shown in Fig. 3. The distributions of all atom–atom distances are provided in the ESI† (Fig. S3). The coordinates of the RMC supercell were collapsed back into a single unit cell and the atoms belonging to the same crystallographic orbit were averaged together to produce the first full set of atomic coordinates for arseniosiderite. The structure is provided as a CIF file attached in the ESI† section of this manuscript and is shown in Fig. 4.

It is important to note that the intensity of the PDF falls off at nearly the same rate as would be expected from instrumental dampening alone. While the diffraction data indicates that there is no long-range order between atoms in different layers, the PDF data seems to indicate that there is a regular relationship between the layers most of the time. Taking into account both types of data, a picture emerges of a layered structure in which the layers are related to each in a regular way most of the time, but with an occasional shifting within the  $bc$ -plane to destroy the long-range correlations.

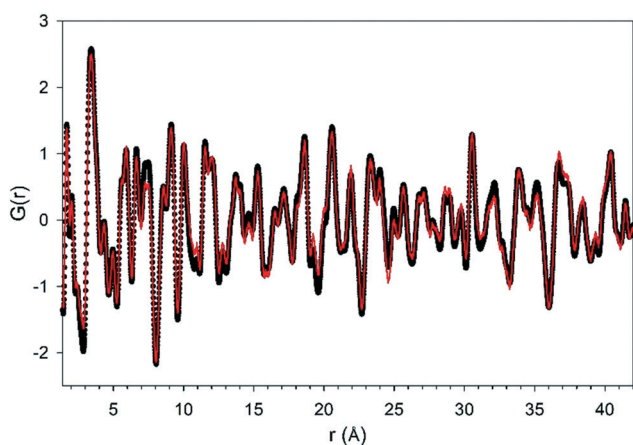


Fig. 3 RMC fit of the LNH arseniosiderite sample. Black circles are data points and the red line is the fit.

### 3.3 PDF analysis of yukonite samples

The PDFs of the yukonite samples bear a strong resemblance to the PDFs of the arseniosiderite samples, confirming a structural relationship (Fig. S4†). The primary difference is that the intensities of the yukonite PDFs fall off more rapidly. There are also some minor differences in the relative intensities. The relative concentration of As–O bond distances compared to Fe–O bond distances are lower in yukonite than arseniosiderite, thus showing yukonite has less  $\text{AsO}_4$  per  $\text{FeO}_6$ . There are also some other notable differences in yukonite, often at points in  $r$  where distances involving Ca contribute heavily, the relative concentrations are lower, hence indicating lower Ca content. Of the four samples measured using the 60 keV photons, three show similar rates of structural correlation decline while one sample (light LNH) shows much stronger correlations at high- $r$  and is

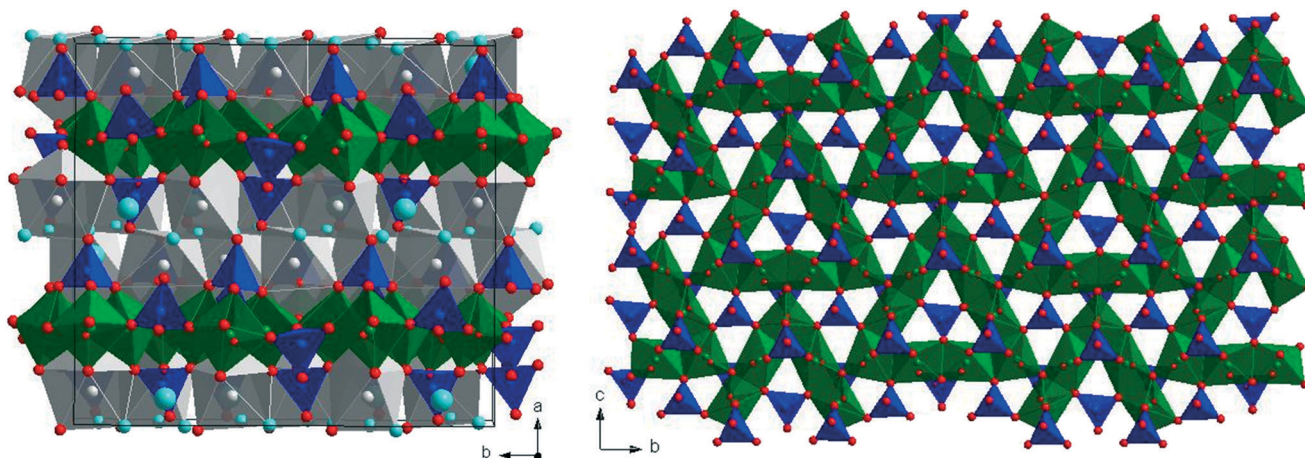


Fig. 4 The structure of arseniosiderite as determined by RMC modeling of PDF data. Green is Fe, blue is As, gray is Ca, red is O except for the O of water molecules which are aqua. H atom positions were not determined. The left figure is one unit cell while the right figure shows the layers of  $\text{FeO}_6$  nonamers connected by  $\text{AsO}_4$ .

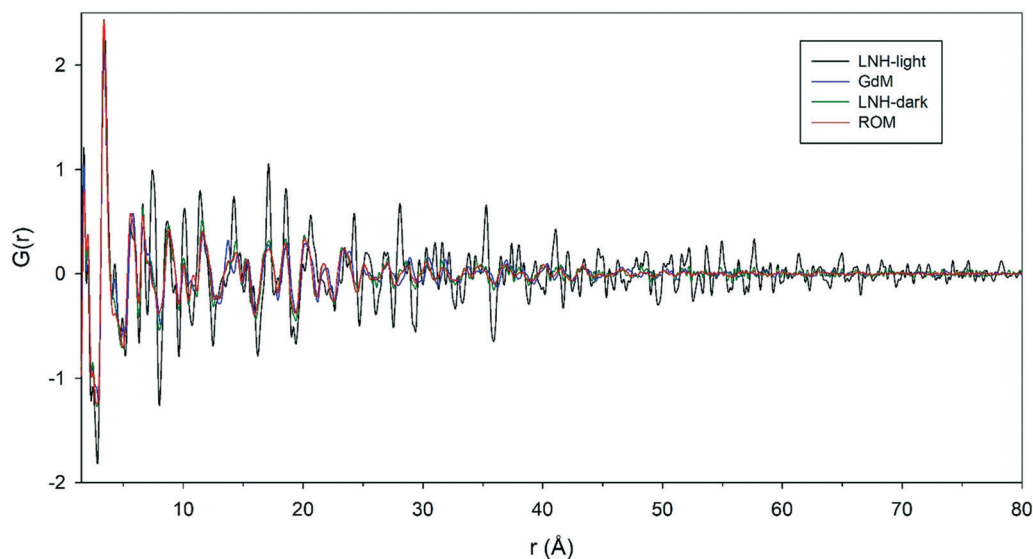


Fig. 5 The PDFs of the 4 yukonite samples measured using 60 keV photons.

between the other yukonite samples and LNH arseniosiderite in terms of correlation length (Fig. 5). The two yukonite samples measured at 115 keV show similar correlation lengths as the 3 samples with shorter correlation lengths measured at 60 keV (Fig. S5†).

How the intensities of the PDFs decline as a function of  $r$  can provide information on the sizes and shapes of the yukonite particles. The fall off of intensity is often described by a shape function. Attempts to model the fall-off using a spherical shape function were highly unsuccessful, suggesting the shapes are highly anisotropic. Several more complex shape functions were also explored but none could provide a good fit. It was noticed that the PDFs display a step-like drop off at several points, which prevents any smooth shape function from modeling them. The relative intensities of the arseniosiderite and yukonite PDFs are similar until  $\sim 3.4$  Å, where the first step-like drop off occurs

(Fig. S4†). This distance is just beyond the Fe–Fe distances that occur between edge-sharing  $\text{FeO}_6$  octahedra. This indicates that nonamers of edge-sharing  $\text{FeO}_6$  still exist in yukonite to roughly the same extent that they do in arseniosiderite, but other cation–cation distances do not retain the same high level of order. Beyond this first drop-off, the intensity of the PDF declines slowly until  $\sim 25$  Å where a second discontinuous drop-off occurs (Fig. 6). At  $\sim 46$  Å a third step-like drop-off is observed. Distances of 25 and 46 Å are just below the longest distances between atoms 2 or 3 nonamers apart which belong to the same sheet of nonamers.

The pattern of the decline in structural correlations seems to show the particles are made of sheets of nonamers which tend to be 2 or 3 nonamers in length but are occasionally longer. The fact that these layers are made of integer numbers of these large structural units causes the step-like

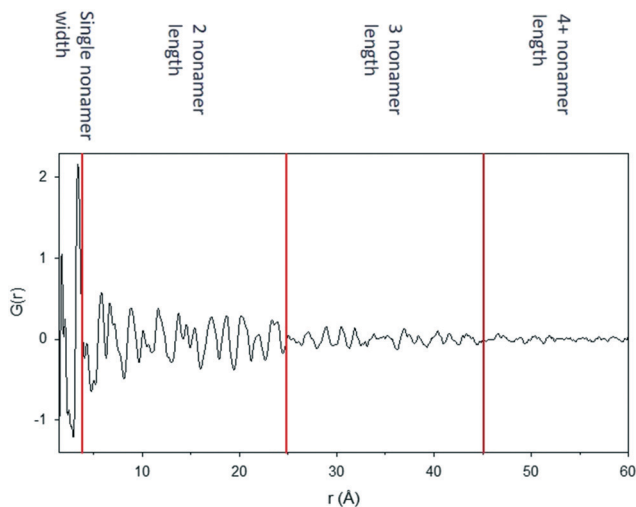


Fig. 6 The PDF of the GdM yukonite sample with the step-like intensity drops-offs labeled.

drop off in the PDFs at longer distances. These sheets can be connected to other sheets through Ca and water but do not tend to stack regularly and there is essentially no structural correlation between layers (Fig. S6†).

### 3.4 TEM analysis of yukonite

Weak crystallinity was observed throughout the LNH yukonite sample. Fig. 7a shows SAED of a region with diffused diffraction rings where no clear plane spacing data can be extracted. Even though the main morphology was sponge-like, a distinct region with crystallinity was also seen (Fig. 7b). High-resolution TEM imaging exhibited two separate planes perpendicular to each other with plane spacings of 11.8 Å and 6.5 Å (Fig. 7c). The determined values *via* HR imaging are lower than the reported *d*-spacings of yukonite planes perpendicular to each other based on hexagonal symmetry ( $d_{001} \sim 15.7$  Å,  $d_{100} \sim 9.8$  Å).<sup>5</sup> However,

it is worth noting that previous authors<sup>5,8,12</sup> have indicated that dehydration under the e-beam can contract the crystal lattice. On the other hand, the 11.8 Å distance is also close to that of the arseniosiderite *c*-axis while the 6.5 Å distance is close to 1/3 the *b*-axis. This supports the conclusion made from PDF data that yukonite has short-range order similar to that seen in the *bc*-plane of arseniosiderite but little structural correlation perpendicular to these layers. Unfortunately, the region was beam-sensitive at 200 kV, hence no SAED was conducted in that region. However, it is worth noting that the distinct region of crystallinity (Fig. 7b) observed was evolving from the amorphous spongy material and whose plane spacing's matched well those observed for arseniosiderite (discussed in the next section). This observation thus provides the first evidence where the evolution of yukonite to arseniosiderite has been observed for a natural specimen.

### 3.5 TEM analysis of arseniosiderite

Particles with sharp edges were mainly observed in the arseniosiderite sample (Fig. 8a) and HR-TEM imaging showed large single-crystalline regions (Fig. 8b). SAED analysis (Fig. 9a) indicated strong diffraction where a hexagonal symmetry was determined ( $\alpha, \beta \sim 60^\circ$ ). A prismatic plane spacing ( $d_{100}$ ) of around 6.6 Å was found (Fig. 9b). HR-TEM imaging indicated planes perpendicular to the prismatic planes, where  $d_{001}$  is determined to be 11.4 Å, in good agreement with PDF results. The observation of hexagonal symmetry is not in contradiction to the diffraction and PDF results. In the monoclinic unit cell used to model the arseniosiderite PDF, the *b*-axis is almost exactly  $\sqrt{3}$  times the *c*-axis, so it is possible to construct a pseudo-trigonal cell with angles close to  $60^\circ$  and  $120^\circ$  by connecting the A-centers. Furthermore, as stated previously, the determined values for the plane spacings of 6.6 Å ( $d_{100}$ ) and 11.4 Å ( $d_{001}$ ), are very similar to the spacings of  $a = 6.5$  Å and  $b = 11.8$  Å observed

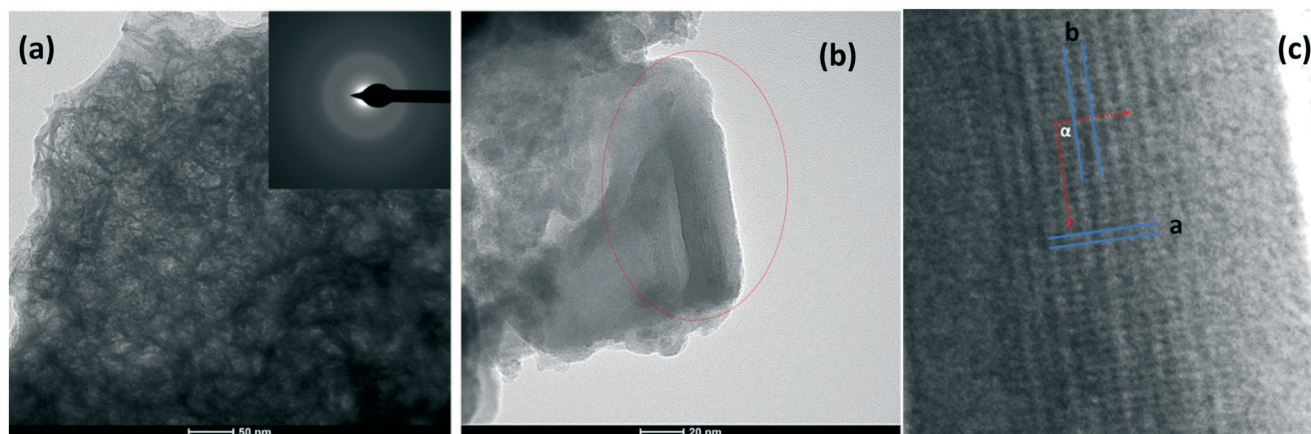


Fig. 7 (a) Bright field images (BFI) exhibiting spongy morphology of the LNH yukonite sample with weak crystallinity (diffused diffraction rings). (b) BFI of a region with distinct morphology containing a single crystal was also observed. (c) Lattice imaging of the region with distinct morphology exhibiting two planes perpendicular to each other ( $\alpha \sim 90^\circ$ ) with plane spacings;  $a = 6.5$  Å and  $b = 11.8$  Å.



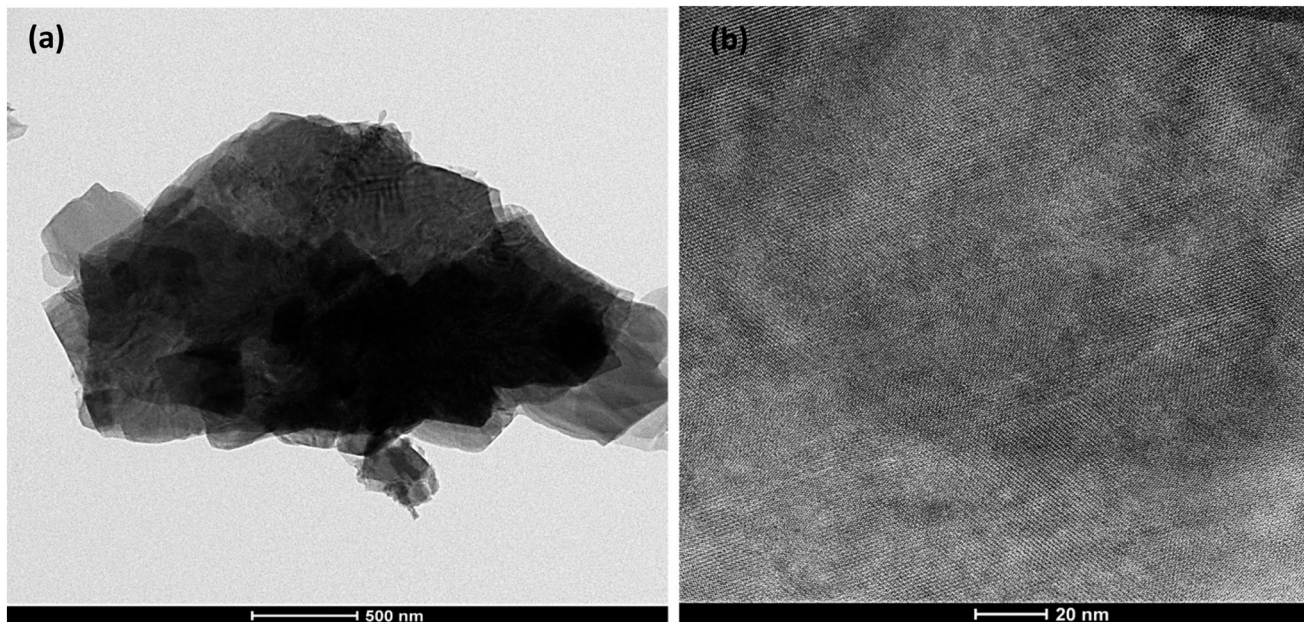


Fig. 8 (a) BFI of LHN arseniosiderite particles with sharp edges and (b) HR-TEM imaging indicating single crystalline lattice.

in the crystalline part evolving from the LNH yukonite (Fig. 7c).

### 3.6 Environmental implications and conclusions

Yukonite and arseniosiderite are important  $\text{Ca(II)-Fe(III)-AsO}_4$  minerals that have been reported to exist in mining ore deposits (e.g. Au, Ag, Zn, Cu, Fe) and mine wastes in 16 different countries worldwide. Their formation has been comprehensively investigated in both synthetic<sup>4,28,32,39</sup> and natural or anthropogenic systems from alterations of arsenopyrite, scorodite, poorly crystalline ferric arsenate, and pharmacosiderite.<sup>1-3,19,28,29</sup> But to date, no complete picture of their key structural components that lead to their formation is known even after 100 years since their discovery.<sup>45</sup> Researchers<sup>1,2,4,16,28</sup> have tried to piece together the key structural components of these minerals *via* the use of various analytical tools (e.g. IR/Raman, lab-XRD, TEM-SAED, X-ray absorption). However, as we have demonstrated

here *via* high energy diffraction, due to the semi-crystalline nature of the arseniosiderite and nano-crystalline nature of yukonite, these analytical tools have failed to fully paint a complete picture of their key structural features and evolution. From the high energy X-ray PDF data, we have observed that the nano-crystalline yukonite is composed of small layers of nonamers  $[\text{Fe}_9\text{O}_6(\text{XO}_4)_9]^{-12}$  (similar to arseniosiderite) that are 2–3 nonamers wide and may be connected through layers containing some Ca and water [possibly as  $\text{Ca}_2\text{O}_{10}(\text{H}_2\text{O})_2$  dimers] but don't stack in any regular way nor does there exist any correlation between the layers. This lack of correlation gives rise to highly anisotropic shape and sizes of the particles as previously observed in TEM studies.<sup>4,5,16,28</sup> Moreover, there appears to exist less  $\text{AsO}_4$  per  $\text{FeO}_6$  and a lower Ca-X content in comparison to arseniosiderite, the latter of which is in agreement with previous chemical composition reports.<sup>4,28</sup> In contrast, arseniosiderite shows a semi-crystalline nature (unlike crystalline mitridatite and robertsite) as its X-ray PDF extends to at least 100 Å and has a high interlayer order that occurs along one direction [100]. This interlayer order along one direction gives rise to the sharp plate-like morphology observed here *via* TEM and previously reported.<sup>4</sup> However, its long-range order is distorted from nanomer layers being shifted in the *bc*-plane but its medium-range order (observed *via* X-ray PDF) indicates it possesses regular interlayer spacings and has a similar structure to mitridatite. Therefore, based on this structural information gathered here we can begin to fully understand how yukonite evolves to arseniosiderite as we have observed here in the LNH natural sample *via* TEM. We can postulate that first, an initial completely nano-amorphous precursor forms where these nonamers or smaller units<sup>28</sup> and layers containing some Ca

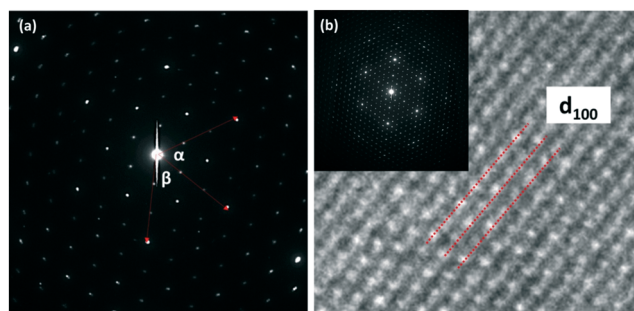


Fig. 9 (a) SAED of arseniosiderite with hexagonal symmetry ( $\alpha, \beta \sim 60^\circ$ ), (b) HR-TEM image of a hexagonal lattice (prismatic planes) with corresponding SAED.

and water [possibly as  $\text{Ca}_2\text{O}_{10}(\text{H}_2\text{O})_2$  dimers] are completely randomly distributed with no order (so-called amorphous matrix often observed *via* TEM). Then as these nonamers start coming together to form small layers that are  $\sim 2\text{--}3$  nonamers in width and are connected in a non-regular way with the Ca-dimers, yukonite anisotropic particles form. At that time as more  $\text{AsO}_4$  is incorporated to join the 9-member  $\text{FeO}_6$  rings to hold more nonamers together and as more Ca-dimers are incorporated to join these layers ( $\parallel$ ) to the *a*-axis, these stack together to give order along 1 single direction (*i.e.* [100]). However, along the way, some of these layers become shifted along the *bc*-plane which distorts the overall long-range order, and the formation of the semi-crystalline arseniosiderite occurs.

The stability in terms of As released into the aqueous environment of mineral phases formed naturally or anthropogenically (*e.g.* hydrometallurgical operations) can be directly related to its crystallinity and the type of specific crystal structure it possesses along with other factors (*e.g.* pH,  $E_h$ , TOC, oxi-suboxic-anoxic, *etc.*). For example, crystalline scorodite is 100 times more stable than its semi-crystalline counterpart (poorly crystalline ferric arsenate).<sup>46–49</sup> The As stability of natural yukonite and arseniosiderite was first reported by Krause and Ettl<sup>46</sup> which indicated them to have similar stability from tests conducted after 197 days without pH control. Swash and Monhemius<sup>50</sup> conducted TCLP-like tests on natural samples and reported that after 7 days, arseniosiderite was more stable than yukonite in the pH range from 3–11. This was further confirmed by Becze and Demopoulos<sup>39</sup> on synthetic samples and TCLP-like testing. In accordance, Paktunc *et al.*<sup>28</sup> computed that arseniosiderite should also exhibit a lower As solubility *vs.* yukonite. Furthermore, Drahotka *et al.*<sup>21</sup> demonstrated that under natural settings, the extractability of As in oxic cambisol soils, as well as mine waste that was dominated by arseniosiderite, exhibited lower As mobility *vs.* those rich in yukonite. Interestingly, Drahotka *et al.*,<sup>19</sup> noted that the presence of arseniosiderite under the high activity of  $\text{Ca(III)}$  from dissolved calcite decreased its As solubility, and this correlated with the high As stability observed in the Mokrsko-west gold deposit. Similarly, synthetic yukonite has been observed to have a substantially improved long term ( $\sim 500$  days) As stability in gypsum saturated solutions at pH 7 (11 orders of magnitude lower), pH 8 (22 orders of magnitude lower), and 9.5 (48 orders of magnitude lower) in comparison to tests done without gypsum.<sup>32,51</sup> It is worth noting that for these synthetic yukonite stability tests, as time proceeded, the calcium concentration in the solutions fluctuated by  $\sim 40\text{--}50 \text{ mg L}^{-1}$  at pH 7–8 while those at pH 9.5 decreased by  $\sim 125 \text{ mg L}^{-1}$ . In contrast, As stability tests done without the presence of gypsum only varied by  $\leq 5 \text{ mg L}^{-1} \text{ Ca(III)}_{(\text{aq})}$ . Thus, based on the gathered data of this work, we can attribute the reported higher As stability of arseniosiderite *vs.* yukonite to its crystallinity where the former is the higher crystalline form of the two. Meanwhile, the higher As stability of yukonite observed in the gypsum saturated tests we can infer

to arise from the uptake of Ca ions from solution to the yukonite nano-crystalline structure. This uptake of Ca ions likely serves to connect more nanomer layers to give it a higher order of crystallinity and stabilize the As units that hold together the sheets of 9 member  $\text{FeO}_6$  rings. Similarly, for arseniosiderite, the presence of an additional source of Ca ions from solution as observed in the natural Mokrsko-west gold deposit<sup>19</sup> likely serves it as aforementioned for yukonite. Namely, to increase its crystallinity and internal order within its semi-crystalline structure. Further work *via* high energy diffraction to solidify these As stability inferences of increased crystallinity and internal order from the uptake of Ca ions in solution into the structures of yukonite and arseniosiderite after stability testing will be undertaken using a similar approach as presented here.

## Conflicts of interest

There are no conflicts of interest to declare.

## Acknowledgements

We would like to thank Robin Hansen and Mike Rumsey, Curators of Minerals at the Natural History Museum London for the donation of the original natural Tagish Lake Yukonite sample and Romanech arseniosiderite. We also kindly thank Professor Gennaro Ventruti from the Università di Bari Aldo Moro for help in obtaining the Italian yukonite samples and Professor George Demopoulos at McGill University for previous guidance and financial support of this research. Matthew Bohan from McGill University is also thanked for useful discussions. MAG kindly thanks Prof. Yongfeng Jia and the National Key R&D Program of China (no. 2017 YFD 0800301) for support. MAG also thanks the National Natural Science Foundation of China (no. 41703129) for financial support. GDV was supported by a grant to the Department of Science, Roma Tre University (MIUR-Italy Dipartimenti di Eccellenza, ARTICOLO 1, COMMI 314 – 337 LEGGE 232/2016). Part of the research described in this paper was performed at the Canadian Light Source, a national research facility of the University of Saskatchewan, which is supported by the Canada Foundation for Innovation (CFI), the Natural Sciences and Engineering Research Council (NSERC), the National Research Council (NRC), the Canadian Institutes of Health Research (CIHR), the Government of Saskatchewan, and the University of Saskatchewan. This research used resources of the Advanced Photon Source, a U.S. Department of Energy (DOE) Office of Science User Facility operated for the DOE Office of Science by Argonne National Laboratory under Contract No. DE-AC02-06CH11357.

## References

- 1 D. Paktunc, A. Foster and G. Laflamme, Speciation and Characterization of Arsenic in Ketza River Mine Tailings Using X-ray Absorption Spectroscopy, *Environ. Sci. Technol.*, 2003, 37, 2067–2074.

- 2 D. Paktunc, A. Foster, S. Heald and G. Laflamme, Speciation and characterization of arsenic in gold ores and cyanidation tailings using X-ray absorption spectroscopy, *Geochim. Cosmochim. Acta*, 2004, **68**, 969–983.
- 3 S. R. Walker, M. B. Parsons, H. E. Jamieson and A. Lanzirrotti, Arsenic Mineralogy Of Near-Surface Tailings And Soils: Influences On Arsenic Mobility And Bioaccessibility In The Nova Scotia Gold Mining Districts, *Can. Mineral.*, 2009, **47**, 533–556.
- 4 M. A. Gomez, L. Becze, R. I. R. Blyth, J. N. Cutler and G. P. Demopoulos, Molecular and structural investigation of yukonite (synthetic & natural) and its relation to arseniosiderite, *Geochim. Cosmochim. Acta*, 2010, **74**, 5835–5851.
- 5 A. Garavelli, D. Pinto, F. Vurro, M. Mellini, C. Viti, T. Balić-Žunić and G. Della Ventura, Yukonite From The Grotta Della Monaca Cave, Sant'agata Di Esaro, Italy: Characterization And Comparison With Cotype Material From The Daulton Mine, Yukon, Canada, *Can. Mineral.*, 2009, **47**, 533–556.
- 6 B. Cancès, F. Juillot, G. Morin, V. Laperche, D. Polya, D. J. Vaughan, J. L. Hazemann, O. Proux, G. E. Brown and G. Calas, Changes in arsenic speciation through a contaminated soil profile: A XAS based study, *Sci. Total Environ.*, 2008, **397**, 178–189.
- 7 A. Bossy, C. Grosbois, S. Beauchemin, A. Courtin-Nomade, W. Hendershot and H. Bril, Alteration of As-bearing phases in a small watershed located on a high grade arsenic-geochemical anomaly (French Massif Central), *Appl. Geochem.*, 2010, **25**, 1889–1901.
- 8 P. J. Dunn, New data for pitticite and a second occurrence of yukonite at Sterling Hill, New Jersey, *Mineral. Mag.*, 1982, **46**, 261–264.
- 9 T. L. Burlak, *M. Sc. Thesis*, California State University, 2012.
- 10 C. S. Kim, D. H. Stack and J. J. Rytuba, Fluvial transport and surface enrichment of arsenic in semi-arid mining regions: examples from the Mojave Desert, California, *J. Environ. Monit.*, 2012, **14**, 1798–1813.
- 11 A. L. Foster, R. P. Ashley and J. J. Rytuba, Arsenic species in weathering mine tailings and biogenic solids at the Lava Cap Mine Superfund Site, Nevada City, CA, *Geochem. Trans.*, 2011, **12**, 1–21.
- 12 D. R. Ross and J. E. Post, New data on yukonite, *Powder Diffr.*, 1997, **12**, 113–116.
- 13 A. Pieczka, B. Golebiowska and W. Franus, Yukonite, a rare Ca-Fe arsenate, from Redziny (Sudetes, Poland), *Eur. J. Mineral.*, 1998, **10**, 1367–1370.
- 14 L. M. C. Candeias, *Ph. D. Thesis*, Universidade do Porto, 2013.
- 15 R. P. Borba and B. R. Figueiredo, The Influence of Geochemical Conditions on Arsenopyrite Oxidation and on the Mobility of Arsenic in Tropical Surface Environments, *Rev. Bras. Geocienc.*, 2004, **34**, 489–500.
- 16 O. Nishikawa, V. Okrugin, N. Belkova, I. Saji, K. Shiraki and K. Tazaki, Crystal symmetry and chemical composition of yukonite: TEM study of specimens collected from Nalychevskie hot springs, Kamchatka, Russia and from Venus Mine, Yukon Territory, Canada, *Mineral. Mag.*, 2006, **70**, 73–81.
- 17 L. A. Dimuccio, N. Rodrigues, F. Larocca, J. Pratas, A. M. Amado and L. A. E. Batista de Carvalho, Geochemical and mineralogical fingerprints to distinguish the exploited ferruginous mineralisations of Grotta della Monaca (Calabria, Italy), *Spectrochim. Acta, Part A*, 2017, **173**, 704–720.
- 18 A. Surour, A. H. Ahmed and H. M. Harbi, Yukonite-like alteration products (Ca-Fe arsenate and As-rich Fe-oxyhydroxide) formed by in situ weathering in granodiorite, Bi'r Tawilah gold prospect, Saudi Arabia, *Eur. J. Mineral.*, 2012, **25**, 61–70.
- 19 P. Drahotka, J. Rohovec, M. Filippi, M. Mihaljevič, P. Rychlovský, V. Červený and Z. Pertold, Mineralogical and geochemical controls of arsenic speciation and mobility under different redox conditions in soil, sediment and water at the Mokrsko-West gold deposit, Czech Republic, *Sci. Total Environ.*, 2009, **407**, 3372–3384.
- 20 P. Drahotka, K. Raus, E. Rychlikova and J. Rahovec, Bioaccessibility of As, Cu, Pb, and Zn in mine waste, urban soil, and road dust in the historical mining village of Kank, Czech Republic, *Environ. Geochem. Health*, 2017, **40**, 1495–1512.
- 21 P. Drahotka, O. Kulakowski, A. Culka, M. Knappova, J. Rohovec, F. Veselovsky and M. Racek, Arsenic mineralogy of near-neutral soils and mining waste at the Smolotely-Lisnice historical gold district, Czech Republic, *Appl. Geochem.*, 2018, **89**, 243–254.
- 22 M. Filippi, B. Doušová and V. Machovič, Mineralogical speciation of arsenic in soils above the Mokrsko-west gold deposit, Czech Republic, *Geoderma*, 2007, **139**, 154–170.
- 23 M. Khorasanipour and E. Esmaeilzadeh, Geo-genic arsenic contamination in the Kerman Cenozoic Magmatic Arc, Kerman, Iran: Implications for the source identification and regional analysis, *Appl. Geochem.*, 2015, **63**, 610–622.
- 24 O. Kodirov, M. Kersten, N. Shukurov and F. J. M. Peinado, Trace metal(loid) mobility in waste deposits and soils around Chadak mining area, Uzbekistan, *Sci. Total Environ.*, 2018, **622–623**, 1658–1667.
- 25 S. Enju and S. Uehara, Yukonite and wallkilldellite-(Fe) from the Kiura mine, Oita Prefecture, Japan, *J. Mineral. Petrol. Sci.*, 2015, **110**, 150–155.
- 26 C. J. Ollson, E. Smith, K. G. Scheckel, A. Betts and A. L. Juhasz, Assessment of arsenic speciation and bioaccessibility in mine-impacted materials, *J. Hazard. Mater.*, 2016, **313**, 130–137.
- 27 K. R. Malloch, D. Craw and D. Trumm, Arsenic mineralogy and distribution at the historic Alexander gold mine, Reefton goldfield, New Zealand, *N. Z. J. Geol. Geophys.*, 2017, **60**, 129–144.
- 28 D. Paktunc, J. Majzlan, A. Huang, Y. Thibault, M. B. Johnson and M. A. White, Synthesis, characterization, and thermodynamics of arsenates forming in the Ca-Fe(III)-As(V)-NO<sub>3</sub> system: Implications for the stability of Ca-Fe arsenates, *Am. Mineral.*, 2015, **100**, 1803–1820.

- 29 P. Drahota and M. Filippi, Secondary arsenic minerals in the environment: A review, *Environ. Int.*, 2009, **35**, 1243–1255.
- 30 Y. Jia and G. P. Demopoulos, Coprecipitation of arsenate with iron(III) in aqueous sulphate media: Effect of time, lime as base and co-ions on arsenic retention, *Water Res.*, 2008, **42**, 661–668.
- 31 M. C. Bluteau, L. Becze and G. P. Demopoulos, The dissolution of scorodite in gypsum-saturated waters: Evidence of Ca–Fe–AsO<sub>4</sub> mineral formation and its impact on arsenic retention, *Hydrometallurgy*, 2009, **97**, 221–227.
- 32 M. T. Bohan, *M. Eng. Thesis*, McGill University, 2014.
- 33 A. M. Nazari, R. Radzinski and A. Ghahreman, Review of arsenic metallurgy: Treatment of arsenic minerals and the immobilization of arsenic, *Hydrometallurgy*, 2017, **174**, 258–281.
- 34 J. Majzlan, P. Drahota and M. Filippi, Parageneses and Crystal Chemistry of Arsenic Minerals, *Rev. Mineral. Geochem.*, 2014, **79**, 17–184.
- 35 P. B. Moore and T. Araki, Mitridatite, Ca<sub>6</sub>(H<sub>2</sub>O)<sub>6</sub>[Fe<sub>9</sub><sup>III</sup>O<sub>6</sub>(PO<sub>4</sub>)<sub>9</sub>]·3H<sub>2</sub>O. A noteworthy octahedral sheet structure, *Inorg. Chem.*, 1977, **16**, 1096–1106.
- 36 M. B. Andrade, S. M. Morrison, A. J. S. Domizio, M. N. Feinglos and R. T. Downs, Robertsite, Ca<sub>2</sub>Mn<sup>III</sup><sub>3</sub>O<sub>2</sub>(PO<sub>4</sub>)<sub>3</sub>·3H<sub>2</sub>O, *Acta Crystallogr., Sect. E: Struct. Rep. Online*, 2012, **68**, i74–i75.
- 37 P. B. Moore, J. Ito and I. Jahnsite, Segelerite, and Robertsite, Three New Transition Metal Phosphate Species II. Redefinition of Overite, and Isotype of Segelerite III. Isotypy of Robertsite, Mitridatite and Arseniosiderite, *Am. Mineral.*, 1974, **59**(1–2), 48–59.
- 38 P. B. Moore and T. Araki, Mitridatite: a remarkable octahedral sheet structure, *Mineral. Mag.*, 1977, **41**, 527–528.
- 39 L. Becze and G. P. Demopoulos, Hydrometallurgical synthesis and stability evaluation of Ca-Fe-AsO<sub>4</sub> compounds, in *The Minerals, Metals & Materials Society, in Extraction and Processing: Proceedings of Symposium*, ed. B. Davis and M. Free, John Wiley & Sons, New Jersey, 2007, pp. 11–18.
- 40 B. H. Toby and R. B. Von Dreele, GSAS-II: the genesis of a modern open-source all purpose crystallography software package, *J. Appl. Crystallogr.*, 2013, **46**, 544–549.
- 41 C. L. Farrow, P. Juhás, J. W. Liu, D. Bryndin, E. S. Božin, J. Bloch, Th. Proffen and S. J. L. Billinge, PDFfit2 and PDFgui: computer programs for studying nanostructure in crystals, *J. Phys.: Condens. Matter*, 2007, **19**, 335219.
- 42 M. G. Tucker, D. A. Keen, M. T. Dove, A. L. Goodwin and Q. Hui, RMC Profile: reverse Monte Carlo for polycrystalline materials, *J. Phys.: Condens. Matter*, 2007, **19**, 335218.
- 43 A. Altomare, N. Corriero, C. Cuocci, A. Falcicchio, A. Moliterni and R. Rizzi, OChemDb: the free online Open Chemistry Database portal for searching and analysing crystal structure information, *J. Appl. Crystallogr.*, 2018, **51**, 1229–1236.
- 44 R. D. Shannon, Revised effective ionic radii and systematic studies of interatomic distances in halides and chalcogenides, *Acta Crystallogr., Sect. A: Cryst. Phys., Diffraction, Theor. Gen. Crystallogr.*, 1976, **32**, 751–767.
- 45 J. B. Tyrrell and R. P. D. Graham, Yukonite, a new hydrous arsenate of iron and calcium, from Tagish Lake, Yukon Territory, Canada: with a note on the associated symplectite, *Proc. Trans. R. Soc. Can.*, 1913, **7**, 1–9.
- 46 E. Krause and V. A. Ettl, Solubilities and stabilities of ferric arsenate compounds, *Hydrometallurgy*, 1989, **22**, 311–337.
- 47 D. Langmuir, J. Mahoney and J. Rowson, Solubility products of amorphous ferric arsenate and crystalline Scorodite (FeAsO<sub>4</sub>·2H<sub>2</sub>O) and their application to arsenic behavior in buried mine tailings, *Geochim. Cosmochim. Acta*, 2006, **70**, 2942–2956.
- 48 M. C. Bluteau and G. P. Demopoulos, The incongruent dissolution of scorodite - Solubility, kinetics and mechanism, *Hydrometallurgy*, 2007, **87**, 163–177.
- 49 J. F. Le Berre, R. Gauvin and G. P. Demopoulos, Characterization of Poorly-Crystalline Ferric Arsenate Precipitated from Equimolar Fe(III)-As(V) Solutions in the pH Range 2 to 8, *Metall. Mater. Trans. B*, 2007, **38**, 751–762.
- 50 P. Swash and A. Monhemius, Hydrothermal precipitation from aqueous solutions containing iron(III), arsenate and sulphate, *Hydrometallurgy*, New York, 1994, pp. 177–190.
- 51 L. Becze, M. A. Gomez, V. Petkov, J. N. Cutler and G. P. Demopoulos, The potential arsenic retention role of Ca-Fe(III)-AsO<sub>4</sub> compounds in lime neutralized co-precipitation tailings, in *Uranium 2010*, ed. E. K. Lam, J. W. Rowson and E. Özberk, CIM, 2010, vol. II, pp. 327–333.